

CLIP-GUIDED UNSUPERVISED SEMANTIC-AWARE EXPOSURE CORRECTION

Puzhen Wu^{1,2}Han Weng²Quan Zheng¹
Jiahui Han²Yi Zhan³
Rui Xu³Hewei Wang²Yiming Li²¹Institute of Software, Chinese Academy of Sciences²Beijing-Dublin International College, University College Dublin³School of Computer Science, Peking University

puzhenwu8@connect.hku.hk

ABSTRACT

Improper exposure often leads to severe loss of details, color distortion, and reduced contrast. Exposure correction still faces two critical challenges: (1) the ignorance of object-wise regional semantic information causes the color shift artifacts; (2) real-world exposure images generally have no ground-truth labels, and its labeling entails massive manual editing. To tackle the challenges, we propose a new unsupervised semantic-aware exposure correction network. It contains an adaptive semantic-aware fusion module, which effectively fuses the semantic information extracted from a pre-trained Fast Segment Anything Model into a shared image feature space. Then the fused features are used by our multi-scale residual spatial mamba group to restore the details and adjust the exposure. To avoid manual editing, we propose a pseudo-ground truth generator guided by CLIP, which is fine-tuned to automatically identify exposure situations and instruct the tailored corrections. Also, we leverage the rich priors from the FastSAM and CLIP to develop a semantic-prompt consistency loss to enforce semantic consistency and image-prompt alignment for unsupervised training. Comprehensive experimental results illustrate the effectiveness of our method in correcting real-world exposure images and outperforms state-of-the-art unsupervised methods both numerically and visually.

Index Terms— Exposure Correction, Exposure Consistency, Unsupervised Learning

1. INTRODUCTION

Real-world imaging is often constrained by diverse environmental lighting and improper camera exposure settings (e.g., aperture, shutter speed, and ISO), leading to exposure issues in images. These problems result in diminished detail, color distortion, and reduced contrast, significantly degrading both image quality and visual appeal. Manual exposure adjustment, however, is time-consuming and labor-intensive, highlighting the need for an automated exposure correction method that can effectively enhance the visibility of image details and improve overall image quality.

Recently, many deep learning methods [1, 2, 3] have been proposed for exposure correction, yet two challenges persist. (1) Most approaches apply global adjustments [1, 3, 2] or coarse binary masks [2], ignoring region-level semantics; this breaks semantic consistency, degrades structural fidelity, and induces color shifts. (2) Many rely on supervised learning [2, 3, 1], requiring expert-edited targets that are costly and subjective, yielding small labeled datasets and poor generalization to real-world unlabeled images.

For the first challenge, We leverage semantic features extracted from the Fast Segment Anything Model (FastSAM) [4] to effec-

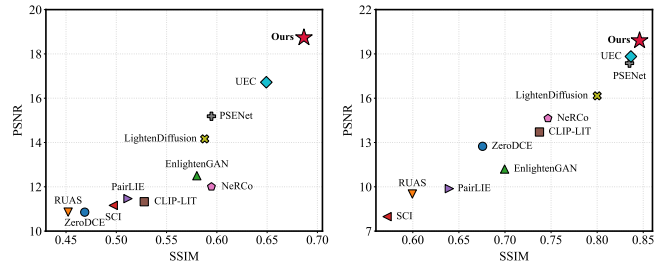


Fig. 1: Performance comparison with other unsupervised methods.

tively introduce object-level semantic priors, by which object-wise regional exposure variations can be well captured. Further, we introduce a new semantic-aware exposure correction network. It consists of multi-scale Semantics-Informed Mamba Reconstruction (SIMR) blocks with downsampling and upsampling operations. Within each SIMR block, we design an Adaptive Semantic-Aware Fusion (ASF) module to fuse the semantic features with image-space features. Following the ASF module, we devise a Residual Spatial Mamba Group (RSMG) module to refine exposure correction with capturing long-range spatial dependencies. To tackle the second challenge, we introduce a CLIP-guided pseudo-ground truth (GT) generator. It employs fine-tuned CLIP [5] prompts to automatically classify exposed images into different exposure situations, which then guide the tailored gamma corrections to form pseudo well-exposed GT. By leveraging pseudo-GT, we eliminate laborious manual labeling. Additionally, we design a new semantic-prompt consistency loss to promote semantic consistency in the semantic space, and push the results of our unsupervised correction towards the well-exposed images in the vision-language joint space. Extensive experiments verify that our method outperforms SOTA unsupervised methods in quantitative metrics (Fig. 1), highlighting its effectiveness for exposure correction. Our main contributions are threefold:

- We propose a novel semantic-aware exposure correction network, which achieves semantics-informed reconstruction with SIMR modules by effectively introducing object-level semantic priors.
- We design an automated pseudo-GT generation approach, eliminating the need for laborious manual labeling.
- We propose a loss that enforces semantic consistency and image-prompt alignment for high-quality unsupervised training.

2. RELATED WORK

Traditional Methods. Early approaches enhance contrast via histogram equalization and gamma correction, or use Retinex-based de-

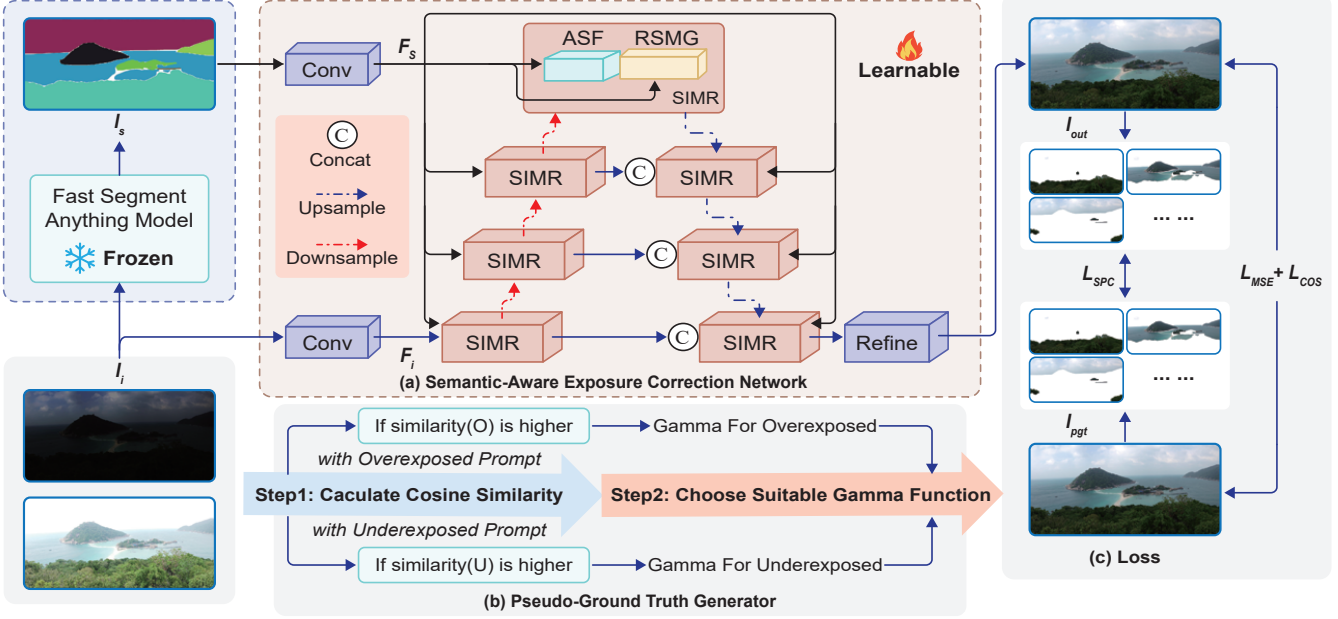


Fig. 2: Overview of our framework: (a) The semantic-aware exposure correction network. (b) Pseudo-ground truth generator. (c) Loss.

composition of illumination/reflectance [6]. While effective in specific cases, these hand-crafted priors often yield artifacts and lack robustness across diverse scenes.

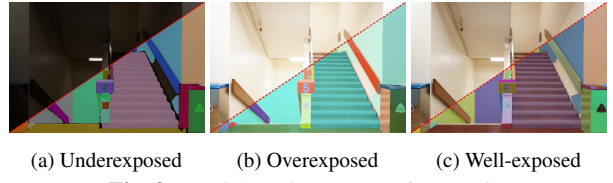
Supervised Learning-based Methods. Supervised methods tackle under/over exposure [2, 3, 1] or focus on low-light [7, 8, 9, 10, 11], but can suffer content loss and color shifts [7]. Representative designs include Laplacian pyramids [12], exposure-consistency modules [13], generative priors, exposure-invariant spaces, and spatial-frequency interactions [1]. Recent low-light enhancement works also emphasize efficient and lightweight designs for practical deployment [14], and source-free scene adaptation has been explored to improve robustness across real-world conditions without target labels [15]. However, many still rely on global correction or coarse masks, struggling in mixed-lighting scenes [3]. Wu et al. [16] use semantics but only enhance underexposed regions, while RECNet [2] depends on binary masks.

Unsupervised Learning-based Methods. To avoid costly labels, unsupervised methods [17, 7, 18, 19] mainly target low-light and struggle with overexposure. Related label-free paradigms also include zero-shot adaptive enhancement via Retinex decomposition and curve estimation [20]. PSENet [21] addresses mixed exposures but uses a fixed global parameter, risking artifacts; UEC [22] leverages multi-exposure sequences. These approaches largely ignore region-wise semantics, leading to local color shifts. We instead propose an unsupervised framework that integrates semantic cues with vision-language priors to handle mixed lighting.

3. METHOD

3.1. Semantic-Aware Exposure Correction Network

Our network stacks SIMR blocks (Fig. 2) to perform multi-scale correction via down/up-sampling. Each SIMR contains an Adaptive Semantic-Aware Fusion (ASF, Fig. 4) and a Residual Spatial Mamba Group (RSMG, Fig. 6). ASF injects region-level semantics to model exposure variations, while RSMG applies adaptive local correction to preserve spatial coherence. We obtain semantics with FastSAM (Fig. 3): for an image $I_i \in \mathbb{R}^{H \times W \times 3}$, a segmentation map $I_s = \mathbf{F}_{\text{sam}}(I_i)$ (frozen weights) is computed, then passed through



(a) Underexposed (b) Overexposed (c) Well-exposed

Fig. 3: FastSAM [4] segmentation results.

a convolutional layer to produce semantic features F_s . Downsampled F_s is fed to each SIMR scale (Fig. 2), enabling content-aware exposure adjustment under mixed lighting.

Adaptive Semantic-Aware Fusion Module. As shown in Figure 4, our ASF module takes in the F_i^m and F_s^m , which are the image-space feature and semantic feature for the m -th SIMR scale, respectively. Drawing inspiration from Wu et al. [16], we first employ a cross-attention block for projecting the semantic feature and the image-space feature into a shared feature space. Specifically, the weighted feature map $W_{kv}(LN(F_i^m))$ is element-wise multiplied by the attention map A^m and goes through a convolutional layer to get the intermediate feature F_{med} , where W_{kv} is a convolutional layer and LN is layer normalization. F_{med} and the skip-connected F_i^m are element-wise added and layer-normalized to obtain E_l^m .

To better fuse semantic and image features, we use a spatial-frequency feed-forward block. The *frequency* branch applies FFT to E_l^m , separates amplitude/phase, refines each with two 1×1 convs, then uses Inverse FFT (IFFT) and a conv, with a residual from E_l^m , to yield E_o^m and capture global exposure trends. The *spatial* branch sends E_l^m through three convolutions to model local details. The two outputs are summed and normalized:

$$E_a^m = LN(E_l^m + FP(E_l^m) + SP(E_l^m)), \quad (1)$$

where FP and SP denote the frequency and spatial branches, respectively; E_a^m is then fed to the RSMG.

Residual Spatial Mamba Group. We follow VMamba [23] and remove the S6 in Mamba [24] and incorporate the 2D selective-scan module (2D-SSM), yielding a Vision Mamba Module (VMM;

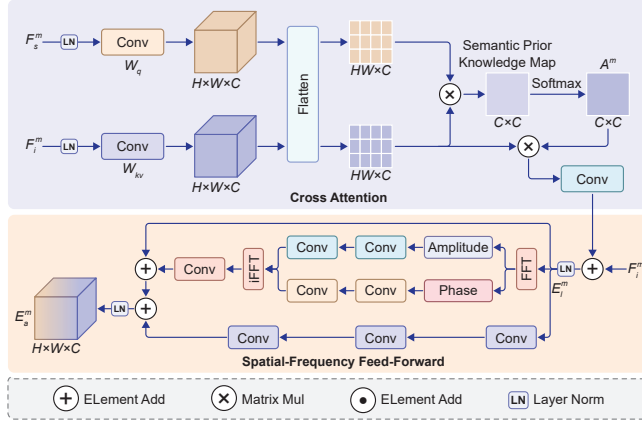


Fig. 4: The architecture of the ASF module.

Fig. 6(c)). Mamba-style architectures have been explored in multiple areas [25, 26]. 2D-SS unfolds a feature map along multiple directions into 1D sequences processed by state-space transitions, then folds them back to 2D, achieving a global receptive field with linear complexity. For exposure correction, this multi-directional modeling captures long-range spatial dependencies. On top of VMM, we propose a Spatial Mamba Block (SMB; Fig. 6(b)) that augments VMM with spatial attention to better handle spatially varying exposures.

We stack multiple Spatial Mamba Blocks (SMBs) into a residual group (RSMG; Fig. 6(a)). For the l -th SMB with input F^l , the upper branch normalizes F^l , applies VMM, a conv, and a linear layer to yield D_1^l ; the lower branch applies normalization, convolutions, spatial attention, and convolutions to produce D_2^l . We fuse them by element-wise addition and add a skip from F^l to obtain $F^{l+1} = F^l + D_1^l + D_2^l$. Stacking SMBs enhances exposure consistency and suppresses color shifts across regions.

3.2. CLIP Guided Pseudo-GT Generation

Prompt Fine-tuning. Inspired by CLIP-LIT [18], we start by initializing three prompts T_w , T_u , and T_o , corresponding to the well-exposed, underexposed, and overexposed conditions. Compared to only learning two prompts (for normal and backlit images) [18], our method extends to three dedicated prompts to better capture the diverse illumination distributions in real scenes. We then fine-tune these prompts using unpaired images from our dataset (see Section 4.1), categorizing them into well-exposed (I_w), underexposed (I_u), and overexposed (I_o) groups. Each image is processed by the pre-trained CLIP image encoder Φ_{image} to produce latent vectors, while the prompts T_w , T_u , and T_o are encoded by the CLIP text encoder Φ_{text} to obtain their latent vectors. Fine-tuning is guided by image-prompt similarity in the shared CLIP latent space, where a triplet cross-entropy loss function $\mathcal{L}_{\text{tune}}$ encourages each prompt to closely align with its matching image category while minimizing similarity with unrelated categories, expressed as:

$$\mathcal{L}_{\text{tune}} = - \sum_{i \in \{w, u, o\}} y_i \cdot \log(\hat{y}_i), \quad (2)$$

$$\hat{y}_i = \frac{\exp(\cos(\Phi_{\text{image}}(I), \Phi_{\text{text}}(T_i)))}{\sum_{j \in \{w, u, o\}} \exp(\cos(\Phi_{\text{image}}(I), \Phi_{\text{text}}(T_j)))}. \quad (3)$$

where $I \in \{I_w, I_u, I_o\}$, y is the label of the current image.

Pseudo-GT Generator. After fine-tuning the underexposed prompts T_u and overexposed prompts T_o , we can calculate the similarity between an input image I and each of these prompts as following:

$$\text{sim}_i = \cos(\Phi_{\text{image}}(I), \Phi_{\text{text}}(T_i)), \quad (4)$$

where $i \in \{u, o\}$. If the similarity between I and T_o is higher than the similarity with the T_u , we decrease the brightness of I . Conversely, if the similarity between I and T_u is higher, we increase the brightness. We leverage an appropriate gamma transformation to produce the pseudo-ground truth image $I_{\text{pgt}} = 1 - (1 - I)^\gamma$, where γ is the factor to either enhance or reduce its brightness.

CLIP Guided Gamma Tuning. Starting from a fixed γ , we refine the γ per image using unpaired data and CLIP’s latent space with the well-exposed prompt T_w . We maximize the similarity between the pseudo-GT and T_w , updating γ by the gradient of this similarity until convergence. This label-free procedure is dataset-agnostic and transferable to other exposure-related tasks.

3.3. Semantic-Prompt Consistency Loss

We propose a Semantic-Prompt Consistency (SPC) loss as an additional objective. SPC combines the Semantic Feature Consistency (SFC) and Image-Prompt Alignment (IPA) losses in a weighted sum as follows:

$$\mathcal{L}_{\text{SPC}} = \beta_1 \mathcal{L}_{\text{SFC}} + \beta_2 \mathcal{L}_{\text{IPA}}, \quad (5)$$

where β_1 and β_2 are balancing weights.

Semantic Feature Consistency Loss. Our SFC loss leverages the semantic prior of the FastSAM to ensure consistency of semantic regions between the output image and the pseudo-GT. Inspired by ECLNet’s [13] treatment of exposure levels as distinct styles, we leverage semantic features and the Gram matrix to ensure consistent exposure correction across semantic regions:

$$\mathcal{L}_{\text{SFC}} = \sum_i \left(\frac{D(h_f^i, h_g^i)}{D(h_f^i, h_g^i) + D(h_f^i, h_l^i)} + \frac{G(h_f^i, h_g^i)}{G(h_f^i, h_g^i) + G(h_f^i, h_l^i)} \right), \quad (6)$$

where D is the L1 distance and G the Gram-matrix difference; h_f^i , h_g^i , and h_l^i are semantic features of the output, pseudo-GT, and input at channel i . The sum runs over all semantic channels.

Image-Prompt Alignment Loss. We introduce IPA loss, leveraging CLIP’s visual-language priors. Specifically, we maximize the cosine similarity between each output image and the fine-tuned well-exposed prompt T_w , while minimizing similarity to overexposed (T_o) and underexposed (T_u) prompts. This encourages the final output to more accurately align with well-exposed characteristics and is expressed as:

$$\mathcal{L}_{\text{IPA}} = \sum_{i \in \{u, o\}} \log(1 + \exp(\text{sim}_i - \text{sim}_w)) \quad (7)$$

Overall Loss Function. We additionally include an MSE term to enforce intensity fidelity and a cosine term to encourage color consistency in sRGB. The complete loss function is expressed as:

$$\mathcal{L}_{\text{TOTAL}} = \lambda_1 \mathcal{L}_{\text{MSE}} + \lambda_2 \mathcal{L}_{\text{COS}} + \lambda_3 \mathcal{L}_{\text{SPC}}, \quad (8)$$

where λ_1 , λ_2 , and λ_3 are the balancing weights.

4. EXPERIMENTS

4.1. Experimental Setup

Datasets. We train on MSEC [12] and SICE [27]. We use only the under-/over-exposed subsets of MSEC (2,830 train / 193 test). For SICE, the 2nd and last levels are treated as under/exposed inputs and a middle level as GT (512 train / 30 test). For prompt fine-tuning, we sample well/under/exposed images from SICE (152/146/161) and MSEC (213/228/205). Moreover, our correction reduces missed detections in low-light face detection (Fig. 8) on DarkFace [28] dataset.

Implementation Details. PyTorch on one NVIDIA A100. Adam ($\beta_1=0.9$, $\beta_2=0.99$), $\text{lr} \times 10^{-4}$, batch 8. Inputs resized to 384x384 with random horizontal/vertical flips.

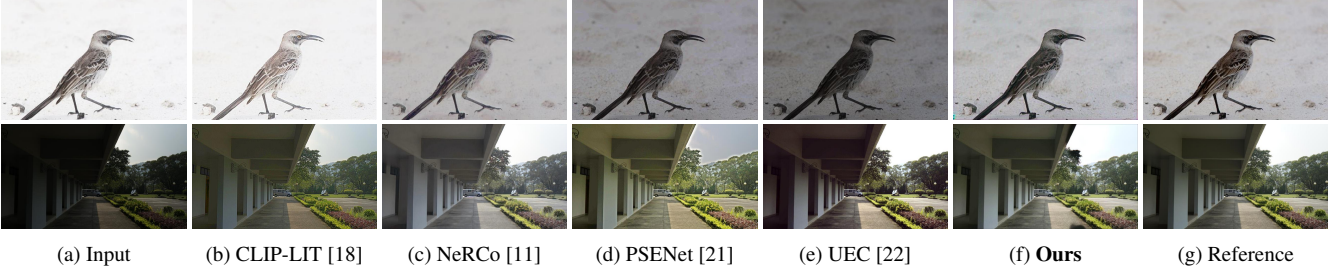


Fig. 5: Qualitative comparison with state-of-the-art unsupervised methods.

| Methods | MSEC [12] | | | | | | SICE [27] | | | | | |
|--------------------------------|----------------|---------------|----------------|---------------|----------------|---------------|----------------|---------------|----------------|---------------|----------------|---------------|
| | Under | | Over | | Average | | Under | | Over | | Average | |
| | PSNR↑ | SSIM↑ |
| ZeroDCE (CVPR20) [7] | 18.2030 | 0.8002 | 7.2810 | 0.5511 | 12.7420 | 0.6757 | 15.7729 | 0.5502 | 5.9362 | 0.3870 | 10.8545 | 0.4686 |
| RUAS (CVPR21) [8] | 13.8135 | 0.7693 | 5.2131 | 0.4296 | 9.5133 | 0.5995 | 16.6306 | 0.5712 | 4.5444 | 0.3330 | 10.5875 | 0.4521 |
| EnlightenGAN (TIP21) [17] | 13.9441 | 0.7567 | 8.4574 | 0.6424 | 11.2008 | 0.6996 | 17.0176 | 0.6453 | 5.9867 | 0.5148 | 11.5022 | 0.5801 |
| SCI (CVPR22) [10] | 10.9230 | 0.6979 | 5.0354 | 0.4463 | 7.9792 | 0.5721 | 17.8687 | 0.6524 | 4.4517 | 0.3416 | 11.1602 | 0.4970 |
| PairLIE (CVPR23) [9] | 12.4261 | 0.7045 | 7.3216 | 0.5748 | 9.8739 | 0.6396 | 16.6697 | 0.6254 | 6.2621 | 0.3978 | 11.4659 | 0.5116 |
| CLIP-LIT (ICCV23) [18] | 17.8663 | 0.8049 | 9.5558 | 0.6699 | 13.7111 | 0.7374 | 15.1130 | 0.6111 | 7.5403 | 0.4445 | 11.3267 | 0.5278 |
| NeRCo (ICCV23) [11] | 18.2953 | 0.7858 | 14.6369 | 0.7344 | 16.4661 | 0.7601 | 18.3092 | 0.6238 | 11.9949 | 0.5163 | 15.1521 | 0.5701 |
| PSENet (WACV2023) [21] | 19.1069 | 0.8382 | 17.6407 | 0.8320 | 18.3738 | 0.8351 | 17.5358 | 0.6490 | 12.5097 | 0.5402 | 15.0228 | 0.5946 |
| LightenDiffusion (ECCV24) [19] | 19.7651 | 0.8418 | 12.5553 | 0.7582 | 16.1602 | 0.8000 | 19.0193 | 0.6757 | 9.3065 | 0.5002 | 14.1629 | 0.5879 |
| UEC (ECCV24) [22] | 18.5293 | 0.8308 | 19.1223 | 0.8424 | 18.8258 | 0.8366 | 16.8998 | 0.6416 | 16.5405 | 0.6568 | 16.7202 | 0.6492 |
| Ours | 20.0607 | <u>0.8392</u> | 19.8717 | 0.8527 | 19.9662 | 0.8460 | 19.4152 | <u>0.6706</u> | 18.0584 | 0.7006 | 18.7368 | 0.6866 |

Table 1: Quantitative comparisons with unsupervised methods. “Under” and “Over” denote the underexposed and overexposed subsets, and “Average” is their mean. Higher PSNR and SSIM indicate better image quality. Best results are shown in **bold** and second-best are underlined.

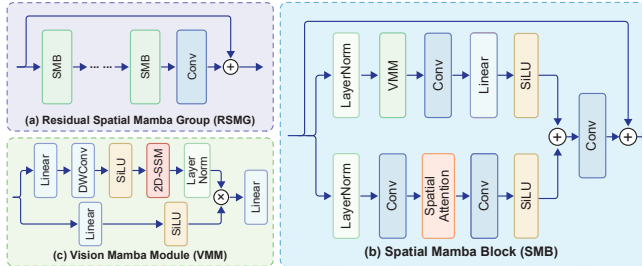


Fig. 6: (a) Residual Spatial Mamba Group (RSMG), (b) Spatial Mamba Block (SMB), (c) Vision Mamba Module (VMM).

| Methods | MSEC [12] | | | SICE [27] | | |
|-------------------|---------------|----------------|---------------|---------------|----------------|---------------|
| | LPIPS (↓) | BRISQUE (↓) | NIMA (↑) | LPIPS (↓) | BRISQUE (↓) | NIMA (↑) |
| ZeroDCE [7] | 0.4348 | 42.8249 | 4.6148 | 0.5271 | 45.2872 | 4.5431 |
| RUAS [8] | 0.5047 | 45.8697 | 4.4174 | <u>0.2461</u> | 25.8244 | 4.8999 |
| EnlightenGAN [17] | 0.3114 | 30.1323 | 4.8953 | 0.3643 | 27.2067 | 4.8252 |
| SCI [10] | 0.3346 | 32.7715 | 4.8284 | 0.7537 | 56.2747 | 4.0070 |
| PairLIE [9] | 0.3871 | 38.7468 | 4.3494 | 0.4318 | 36.5174 | 4.3053 |
| CLIP-LIT [18] | 0.2843 | 32.2784 | 4.6556 | 0.3677 | 31.9127 | 4.4517 |
| NeRCo [11] | 0.3248 | 36.2093 | 4.9761 | 0.4002 | 30.9285 | 4.8740 |
| PSENet [21] | 0.2104 | 30.1071 | 4.9901 | 0.2807 | 30.0326 | 4.7881 |
| LightenDiff [19] | 0.2357 | 29.5824 | 4.9951 | 0.3146 | 22.9735 | 4.4875 |
| UEC [22] | 0.2309 | 35.4327 | 4.9703 | 0.3033 | 27.7842 | 4.9513 |
| Ours | <u>0.2107</u> | 27.6882 | 5.0131 | 0.2117 | 15.8901 | <u>4.9228</u> |

Table 2: Quantitative comparisons in terms of additional metrics.

4.2. Comparisons with State-of-the-art Methods

Quantitative Comparisons. In the comparisons with unsupervised methods (Table 1), our model outperforms nearly all compared methods, including CLIP-LIT [18], PSENet [21], and the recent UEC [22]. Specifically, we achieve substantial improvements over the previous best model, UEC, on two datasets. Then in Table 2, we further provide additional quantitative comparisons of unsupervised methods across multiple metrics, including LPIPS [29], BRISQUE [30], and NIMA [31].

Qualitative Comparisons. Figure 5 presents qualitative comparisons on representative images from the MSEC and SICE datasets

using state-of-the-art unsupervised methods and our approach. Existing methods often struggle under mixed lighting, over-brightening bright regions or oversaturating colors. In contrast, our method restores natural colors and preserves structures while balancing exposure across regions.

| Methods | Under | | Over | | Average | |
|-------------|--------------|--------------|--------------|--------------|--------------|--------------|
| | PSNR | SSIM | PSNR | SSIM | PSNR | SSIM |
| Module | 18.94 | 0.649 | 17.75 | 0.680 | 18.35 | 0.664 |
| w/o ASF | 19.16 | 0.652 | 17.92 | 0.700 | 18.54 | 0.676 |
| Loss | 19.09 | 0.643 | 17.73 | 0.667 | 18.41 | 0.655 |
| w/o SPC | 18.96 | 0.641 | 17.82 | 0.675 | 18.39 | 0.658 |
| w/o IPA | 19.31 | 0.665 | 18.01 | 0.694 | 18.66 | 0.679 |
| w/o COS | | | | | | |
| Ours | 19.41 | 0.671 | 18.06 | 0.703 | 18.74 | 0.687 |

Table 3: Ablation on modules and loss components.

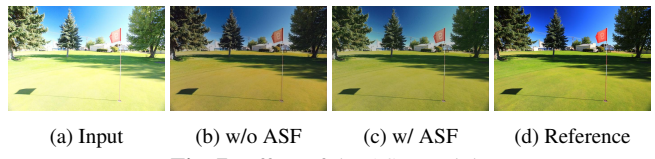


Fig. 7: Effect of the ASF module.

4.3. Ablation Study

We conduct comprehensive ablations on modules and losses in Tables 3 on the SICE dataset [27]. It shows that removing the ASF module causes the largest drop in both PSNR and SSIM, highlighting the importance of semantic-guided feature integration (see Fig. 7). Removing the SpatialAttn branch also degrades performance, confirming the necessity of spatial attention for robust correction under mixed lighting. It further dissects the loss design: discarding SPC or IPA leads to notable declines. Overall, each component contributes meaningfully, and the full model achieves the best scores.

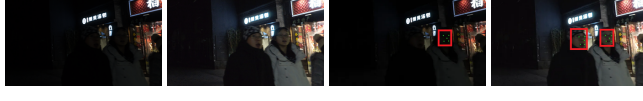


Fig. 8: Face detection results on DarkFace [28] dataset.

5. CONCLUSION

In this work, we propose an unsupervised semantic-aware framework for exposure correction that delivers superior visual quality and improved metric scores. Extensive experiments demonstrate the effectiveness and robustness of our approach. While effective, inference speed slows for very high-resolution inputs. For future work, we plan to leverage generative models for localized inpainting to recover details lost in over/underexposed regions and explore lighter backbones and pruning/distillation to cut latency and memory. Moreover, extending exposure correction to dynamic video and multi-camera settings could benefit from recent advances in camera motion understanding and large-scale camera array calibration [32, 33].

References

[1] Jie Huang, Yajing Liu, Feng Zhao, Keyu Yan, Jinghao Zhang, Yukun Huang, Man Zhou, and Zhiwei Xiong, “Deep fourier-based exposure correction network with spatial-frequency interaction,” in *European Conference on Computer Vision*. Springer, 2022, pp. 163–180.

[2] Jin Liu, Huiyuan Fu, Chuanming Wang, and Huadong Ma, “Region-aware exposure consistency network for mixed exposure correction,” in *Proceedings of the AAAI Conference on Artificial Intelligence*, 2024, vol. 38, pp. 3648–3656.

[3] Yiyu Li, Ke Xu, Gerhard Petrus Hancke, and Rynson WH Lau, “Color shift estimation-and-correction for image enhancement,” in *Proceedings of the IEEE/CVF Conference on Computer Vision and Pattern Recognition*, 2024, pp. 25389–25398.

[4] Xu Zhao, Wenchao Ding, Yongqi An, Yinglong Du, Tao Yu, Min Li, Ming Tang, and Jinqiao Wang, “Fast segment anything,” *arXiv preprint arXiv:2306.12156*, 2023.

[5] Alec Radford, Jong Wook Kim, Chris Hallacy, Aditya Ramesh, Gabriel Goh, Sandhini Agarwal, Girish Sastry, Amanda Askell, Pamela Mishkin, Jack Clark, et al., “Learning transferable visual models from natural language supervision,” in *International Conference on Machine Learning*. PMLR, 2021, pp. 8748–8763.

[6] Edwin H Land, “The retinex theory of color vision,” *Scientific american*, vol. 237, no. 6, pp. 108–129, 1977.

[7] Chunle Guo, Chongyi Li, Jichang Guo, Chen Change Loy, Jun-hui Hou, Sam Kwong, and Runmin Cong, “Zero-reference deep curve estimation for low-light image enhancement,” in *Proceedings of the IEEE/CVF conference on computer vision and pattern recognition*, 2020, pp. 1780–1789.

[8] Risheng Liu, Long Ma, Jiaao Zhang, Xin Fan, and Zhongxuan Luo, “Retinex-inspired unrolling with cooperative prior architecture search for low-light image enhancement,” in *Proceedings of the IEEE/CVF conference on computer vision and pattern recognition*, 2021, pp. 10561–10570.

[9] Zhenqi Fu, Yan Yang, Xiaotong Tu, Yue Huang, Xinghao Ding, and Kai-Kuang Ma, “Learning a simple low-light image enhancer from paired low-light instances,” in *Proceedings of the IEEE/CVF conference on computer vision and pattern recognition*, 2023, pp. 22252–22261.

[10] Long Ma, Tengyu Ma, Risheng Liu, Xin Fan, and Zhongxuan Luo, “Toward fast, flexible, and robust low-light image enhancement,” in *Proceedings of the IEEE/CVF conference on computer vision and pattern recognition*, 2022, pp. 5637–5646.

[11] Shuzhou Yang, Moxuan Ding, Yanmin Wu, Zihan Li, and Jian Zhang, “Implicit neural representation for cooperative low-light image enhancement,” in *Proceedings of the IEEE/CVF international conference on computer vision*, 2023, pp. 12918–12927.

[12] Mahmoud Afifi, Konstantinos G Derpanis, Bjorn Ommer, and Michael S Brown, “Learning multi-scale photo exposure correction,” in *Proceedings of the IEEE/CVF Conference on Computer Vision and Pattern Recognition (CVPR)*, 2021, pp. 9157–9167.

[13] Jie Huang, Man Zhou, Yajing Liu, Mingde Yao, Feng Zhao, and Zhiwei Xiong, “Exposure-consistency representation learning for exposure correction,” in *Proceedings of the 30th ACM International Conference on Multimedia*, 2022, pp. 6309–6317.

[14] Xi Wang and Quan Zheng, “Lightllie: Lightweight low-light image enhancement via dual attention and re-parameterization,” in *2025 International Joint Conference on Neural Networks (IJCNN)*. IEEE, 2025, pp. 1–8.

[15] Xi Wang and Quan Zheng, “Revitalize supervised low-light image enhancer: Learning source-free fast scene adaptation,” in *International Conference on Intelligent Computing*. Springer, 2025, pp. 86–98.

[16] Yuhui Wu, Chen Pan, Guoqing Wang, Yang Yang, Jiwei Wei, Chongyi Li, and Heng Tao Shen, “Learning semantic-aware knowledge guidance for low-light image enhancement,” in *Proceedings of the IEEE/CVF conference on computer vision and pattern recognition*, 2023, pp. 1662–1671.

[17] Yifan Jiang, Xinyu Gong, Ding Liu, Yu Cheng, Chen Fang, Xiaohui Shen, Jianchao Yang, Pan Zhou, and Zhangyang Wang, “Enlightengan: Deep light enhancement without paired supervision,” *IEEE transactions on image processing*, vol. 30, pp. 2340–2349, 2021.

[18] Zhixin Liang, Chongyi Li, Shangchen Zhou, Ruicheng Feng, and Chen Change Loy, “Iterative prompt learning for unsupervised backlit image enhancement,” in *Proceedings of the IEEE/CVF International Conference on Computer Vision*, 2023, pp. 8094–8103.

[19] Hai Jiang, Ao Luo, Xiaohong Liu, Songchen Han, and Shuaicheng Liu, “Lightendiffusion: Unsupervised low-light image enhancement with latent-retinex diffusion models,” in *European Conference on Computer Vision*. Springer, 2024, pp. 161–179.

[20] Yuping Xia, Fanjiang Xu, and Quan Zheng, “Zero-shot adaptive low light enhancement with retinex decomposition and hybrid curve estimation,” in *2023 International Joint Conference on Neural Networks (IJCNN)*. IEEE, 2023, pp. 1–8.

[21] Hue Nguyen, Diep Tran, Khoi Nguyen, and Rang Nguyen, “Psenet: Progressive self-enhancement network for unsupervised extreme-light image enhancement,” in *Proceedings of the IEEE/CVF Winter Conference on Applications of Computer Vision*, 2023, pp. 1756–1765.

[22] Ruodai Cui, Li Niu, and Guosheng Hu, “Unsupervised exposure correction,” in *European Conference on Computer Vision*. Springer, 2024, pp. 252–268.

[23] Yue Liu, Yunjie Tian, Yuzhong Zhao, Hongtian Yu, Lingxi Xie, Yaowei Wang, Qixiang Ye, Jianbin Jiao, and Yunfan Liu, “Vmamba: Visual state space model,” *Advances in neural information processing systems*, vol. 37, pp. 103031–103063, 2024.

[24] Albert Gu and Tri Dao, “Mamba: Linear-time sequence modeling with selective state spaces,” *arXiv preprint arXiv:2312.00752*, 2023.

[25] Puzhen Wu, Hexin Dong, Yi Lin, Yihao Ding, and Yifan Peng, “A disease-aware dual-stage framework for chest x-ray report generation,” *arXiv preprint arXiv:2511.12259*, 2025.

[26] Puzhen Wu, Mingquan Lin, Qingyu Chen, Emily Y Chew, Zhiyong Lu, Yifan Peng, and Hexin Dong, “Amd-mamba: A phenotype-aware multi-modal framework for robust amd prognosis,” in *International Workshop on Machine Learning in Medical Imaging*. Springer, 2025, pp. 150–160.

[27] Jianrui Cai, Shuhang Gu, and Lei Zhang, “Learning a deep single image contrast enhancer from multi-exposure images,” *IEEE Transactions on Image Processing*, vol. 27, no. 4, pp. 2049–2062, 2018.

[28] Wenhan Yang, Ye Yuan, Wenqi Ren, Jiaying Liu, Walter J Scheirer, Zhangyang Wang, Taiheng Zhang, Qiaoyong Zhong, Di Xie, Shiliang Pu, et al., “Advancing image understanding in poor visibility environments: A collective benchmark study,” *IEEE Transactions on Image Processing*, vol. 29, pp. 5737–5752, 2020.

[29] Richard Zhang, Phillip Isola, Alexei A. Efros, Eli Shechtman, and Oliver Wang, “The unreasonable effectiveness of deep features as a perceptual metric,” in *Proceedings of the IEEE/CVF Conference on Computer Vision and Pattern Recognition (CVPR)*, June 2018.

[30] Anish Mittal, Anush Krishna Moorthy, and Alan Conrad Bovik, “No-reference image quality assessment in the spatial domain,” *IEEE Transactions on Image Processing*, vol. 21, no. 12, pp. 4695–4708, 2012.

[31] Hossein Talebi and Peyman Milanfar, “NIMA: Neural image assessment,” *IEEE Transactions on Image Processing*, vol. 27, no. 8, pp. 3998–4011, 2018.

[32] Zhiqiu Lin, Siyuan Cen, Daniel Jiang, Jay Karhade, Hewei Wang, Chanchalik Mitra, Tiffany Ling, Yuhan Huang, Sifan Liu, Mingyu Chen, Rushikesh Zawar, Xue Bai, Yilun Du, Chuang Gan, and Deva Ramanan, “Towards understanding camera motions in any video,” *arXiv preprint arXiv:2504.15376*, 2025.

[33] Jinjiang You, Hewei Wang, Yijie Li, Mingxiao Huo, Long Van Tran Ha, Mingyuan Ma, Jinfeng Xu, Puzhen Wu, Shubham Garg, and Wei Pu, “Multi-Cali Anything: Dense Feature Multi-Frame Structure-from-Motion for Large-Scale Camera Array Calibration,” *arXiv preprint arXiv:2503.00737*, 2025.